Delft University of Technology

Characterization of liners using a lattice-boltzmann solver

Manjunath, Pranav; Avallone, Francesco; Casalino, Damiano; Ragni, Daniele; Snellen, Mirjam

Important note
To cite this publication, please use the final published version (if applicable).
Please check the document version above.

Characterization of Liners using a Lattice-Boltzmann Solver

Pranav Manjunath*, Francesco Avallone [†], Damiano Casalino [‡], Daniele Ragni [§] and Mirjam Snellen [¶]

Delft University of Technology, Kluyverweg 1, 2629HS, Delft, The Netherlands

Acoustic liners are widely used as noise suppression devices, for example in aircraft engines. The effectiveness of the liners is measured through the impedance. In the present study, using a lattice-Boltzmann solver, the response of two liner geometries to grazing acoustic waves is examined. The two geometries have porosity equal to 0.99% and 6.89%, respectively. Impedance is computed using the traditional in-situ method. The results from the simulation are validated against previous experimental data, DNS data and predictions from semi-empirical models. Results show agreement with these reference data, allowing to use the computational setup for further analysis with a realistic liner configuration in the presence of a grazing flow.

I. Nomenclature

A	=	Orifice area
C_D	=	Discharge coefficient
c_i	=	Discrete velocity component in the ith direction
c_∞	=	Speed of sound
d	=	Diameter of the orifice
f	=	Acoustic frequency
f_i	=	Particle density distribution function in the ith direction
h	=	Cavity depth
J_i	=	Bessel's function of the first kind
k_a	=	Acoustic wave number
k_s	=	Stokes wave number
N	=	Number of voxels per orifice diameter
p	=	Static pressure
$\hat{p}$	=	Complex-valued Fourier coefficients of the acoustic pressure
R	=	Acoustic resistance
r	=	Radius of the orifice
t_f	=	Thickness of the facesheet
u_τ	=	Frictional wall velocity
V	=	Volume of the cavity
v	=	Acoustic particle velocity
$\hat{v}$	=	Complex-valued Fourier coefficients of the acoustic velocity
w_i	=	Discrete weight function in the ith direction
X	=	Acoustic reactance
Z	=	Acoustic impedance
χ	=	Normalised acoustic reactance
Δt	=	Numerical time step
μ	=	Dynamic viscosity of air
ν	=	Kinematic viscosity
Ω_i	=	Discrete collision component in the ith direction
ω	=	Acoustic angular frequency
ρ	=	Density

*PhD Researcher, Department of Aerodynamic, Wind Energy and Propulsion, p.manjunath@tudelft.nl

[†] Assistant Professor, Department of Aerodynamic, Wind Energy and Propulsion, f.avallone@tudelft.nl, AIAA member

[‡] Professor, Department of Aerodynamic, Wind Energy and Propulsion, d.casalino@tudelft.nl, AIAA member

[§] Assistant Professor, Department of Aerodynamic, Wind Energy and Propulsion, d.ragni@tudelft.nl, AIAA member

[¶] Associate Professor, Department of Aircraft Noise and Climate Effect, m.snellen@tudelft.nl

σ	=	Porosity
τ_w	=	Wall shear stress
θ	=	Normalised acoustic resistance

II. Introduction

Acoustic liners are widely used as surface treatment devices to suppress noise. In aircraft, reducing engine noise is essential to meet the stringent noise regulations being adopted across the globe [1]. Liners are placed on the walls of the intake and the by-pass ducts. For the new ultra high bypass ratio engines, modifications in the design have resulted in a change in the required surface treatment dimensions [2] and the current liner geometry might no longer be effective. On the other hand, liners can also be used for example in a closed test-section wind tunnel to reduce the background noise. Thus, insights into the liners behaviour will be crucial for an optimal design to achieve the maximum noise suppression.

Depending on their structure, acoustic liners are classified as either locally or non-locally reacting [3]. Typically, locally reacting liners are made up of an array of cells known as Helmholtz resonators, such that there is no interaction between the individual cells. On the other hand, non-locally reacting liners are made up of metallic foam or porous material, with the possibility of interaction of the acoustic waves inside the material. Alternately, based on the effective noise suppression range, it is possible to classify liners as: single degree of freedom (SDOF), double degree of freedom (DDOF) and bulk absorber [3]. Typically, a SDOF liner has a perforated facesheet with a layer of resonator cells/cavity and a solid backplate (see Fig.1). The DDOF liner is similar to a SDOF liner but adds a second layer of septum sheet (mid-sheet) in-between the facesheet and backplate. Bulk absorbers, in contrast, are characterised by a single layer of porous material in-between the facesheet and the backplate. A SDOF liner is effective only over a narrow frequency range. The DDOF is effective over a wider frequency range, whereas the bulk absorber is effective over a broadband frequency range.
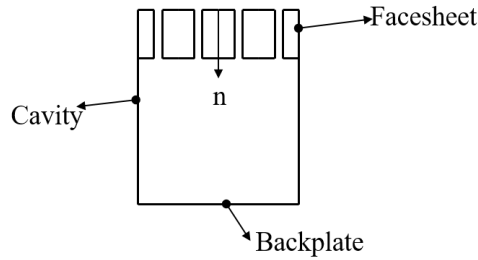

Fig. 1   Illustration of single degree of freedom liner.

The SDOF liners are most commonly used and in principle, they reduce the amplitude of the incident sound wave by converting a part of the incident acoustic energy into (1) energy associated with vorticity and (2) scattering it into spherical acoustic field [4]. The performance of a liner is characterised by its impedance (Z), defined as:

$$Z = \frac{\hat{p}}{\hat{\mathbf{v}} \cdot \mathbf{n}} \tag{1}$$

where $\hat{p}$ and $\hat{\mathbf{v}}$, respectively, are the complex-valued Fourier coefficients of the acoustic pressure and acoustic particle velocity at the surface of the liner and $\mathbf{n}$ represents the wall normal direction, defined as in Fig. 1. The real and imaginary parts of impedance are referred to as resistance (R) and reactance (X), respectively. Physically, resistance is associated with the energy loss mechanisms such as the pressure loss across the orifice, due to the frictional forces and the generation of eddies at the tips of the orifice. This was first demonstrated by Sivian [5] based on the measured velocity dependence of the resistance. Ingard et al. [6] experimentally studied the flow-field around an orifice and presented evidence of the formation of a vortex ring in addition to the presence of a jet-like flow through the orifice. On the other hand, reactance is associated with the inertia of the medium. It can be decomposed into two components, one due to the cavity and the other due to the mass-flow associated with the orifice [3].

Ingard et al. [6] showed that impedance is dependent on the amplitude and the frequency of the incident sound wave, and orifice geometry (i.e., its diameter and thickness). Depending on the sound pressure level (SPL) of the

2

incident wave, the response of the liner can be either linear (impedance does not change with a change in the SPL of the incident wave) or non-linear (impedance changes with a change in the SPL of the incident wave). Melling [7] studied the response of liners to the SPL of the incident waves. He observed that, for materials commonly used in practice, the non-linear behaviour appears for SPLs above 130 dB. Further, he showed that the non-linear behaviour is dependent on the porosity, the discharge coefficient, and the acoustic particle velocity through the holes of the perforated plate. Among the aforementioned parameters, the discharge coefficient, which is dependent on the hole geometry and the Reynold number of the flow through the hole, is the most crucial.

Studies [7–9] have focused on developing impedance models for acoustic liners based on measured parameters. Melling [7] derived a semi-empirical model to predict the impedance for both the linear and the non-linear regimes without background flow. He based the model on the assumption of a quasi-steady flow (sound-induced) through the orifice. Starting from Crandalls' theory for linear impedance in a single tube [10], Melling considered the end corrections to resistance and reactance given by Sivian [5] and Ingard [6], and derived a term for the non-linear regime. The full impedance model has the following form [7]:

$$\frac{Z}{\rho c_\infty} = \frac{i\omega}{c_\infty \sigma C_D} \left[\frac{t_f}{F(k'_s r)} + \frac{8d\Psi(\zeta)}{3\pi F(k_s r)} \right] + \frac{1.2}{2c_\infty} \frac{1-\sigma^2}{(\sigma C_D)^2} v_{rms} \tag{2}$$

where ρ is the density, c_∞ is the speed of sound, σ is the porosity of the liner, C_D is the discharge coefficient, $\omega = 2\pi f$ is the angular frequency, $r = \frac{d}{2}$ is the radius of the orifice, t_f is the thickness of the facesheet, v_{rms} is the rms of the acoustic velocity , k_s and k'_s are the Stokes wave number in the orifice defined as:

$$k_s = \sqrt{-\frac{i\omega}{\nu}} \quad \text{and} \quad k'_s = \sqrt{-\frac{i\omega}{\nu'}} \tag{3}$$

where $\nu' = 2.179\nu$ is the effective kinematic viscosity, ν is the kinematic viscosity. Further,

$$F(k'_s r) = 1 - \left[\frac{2J_1(k'_s r)}{k'_s r J_0(k'_s r)} \right] \tag{4}$$

In Eq. 4, J_0 and J_1 are the Bessel function of the first kind; $\Psi(\zeta)$ is the Fok function, which accounts for the acoustic interaction between neighbouring orifice, defined as:

$$\Psi(\zeta) = \sum_{n=0}^{n=8} a_n \zeta^n \tag{5}$$

with $\zeta = \sqrt{\sigma}$, $a_0 = 1$, $a_1 = -1.4092$, $a_2 = 0$, $a_3 = 0.33818$, $a_4 = 0$, $a_5 = 0.06793$, $a_6 = -0.02287$, $a_7 = 0.03015$ and $a_8 = -0.01641$. The first term in Eq. 2 represents the linear component of impedance due to flow through the orifice; the second term represents the contribution due to the end-corrections and the effect of acoustic interaction between the different orifices; and the third term represents the contribution of the non-linear resistance.

Another commonly used model for the design of liners without background flow was proposed by Motsinger et al.[3]. This model is given by:

$$\frac{Z}{\rho c_\infty} = \frac{R}{\rho c_\infty} + i\frac{X}{\rho c_\infty} \tag{6}$$

with,

$$\frac{R}{\rho c_\infty} = \frac{32\mu t_f}{\rho c_\infty \sigma C_D d^2} + \frac{1}{2c_\infty (\sigma C_D)^2} v_{rms} \tag{7}$$

and

$$\frac{X}{\rho c_\infty} = \frac{k_a(t_f + \epsilon d)}{\sigma C_D} - cot(k_a h) \tag{8}$$

where k_a is the acoustic wave number, h is the cavity depth and

$$\epsilon = 0.85(1 - 0.7\sqrt{\sigma}) \tag{9}$$

For both the above described models, v_{rms} is unknown until Z is known. Using the relation

$$v_{rms} = \frac{p_{ref} 10^{\frac{SPL}{20}}}{Z} \tag{10}$$

3

Eqs. 2 and 10, and Eqs. 6 and 10 can be iteratively solved to obtain Z for a given SPL of the incident wave with $p_{ref} = 2 \times 10^{-5}$Pa.

Impedance models have proved to be effective tools to quickly characterise the behaviour of the liners. However, in deriving the analytical expressions, assumptions are necessary. These are for example that the sound-induced flow through the orifice is hydrodynamically incompressible, the velocity profile across the orifice can be replaced by an average value and the steady-state and instantaneous acoustic behaviour are equivalent. Kraft et al. [11] showed that, under certain operating conditions, the assumption of quasi-steady behaviour of the liner is not valid. Further, the inclusion of background flow, such as in realistic configurations, makes the derivation of analytical models even more challenging. Therefore, in order to improve the models and define its limitations, a more detailed description of the flow features around the cavity is necessary.

The recent improvements in both experimental and numerical methods have helped in getting a better understanding of the flow features associated with the liners. Tam et al. [12] investigated the sound-induced flow-field around a two-dimensional slit liner using Direct Numerical Simulation (DNS). The results, at low SPL, showed that most of the acoustic damping is due to the shear gradients in the boundary layer of the orifice. This observation is in agreement with previous experiments and theory. However at higher SPL, unlike in Ingard [6], an oscillating turbulent jet is not found to be the most dominant energy dissipation mechanism. In fact, the DNS results indicate that at higher SPL, the shedding of the vortices is the primary source of energy dissipation. Further investigations using experimental flow visualisation by Tam et al. [13] confirmed this phenomenon. Zhang et al. [14] performed DNS on an acoustically excited flow through a circular orifice with a hexagonal cavity. Their results show that, depending on the incident sound wave parameters, secondary vorticity is observed within the orifice boundary layer which increases the non-linear behaviour of the liner. Roche et al. [15] studied the effects of high SPL of the incident waves on the liners using DNS. The study highlighted that at frequencies different from the resonance one, an increase in SPL results in increasing the energy dissipation. On the other hand, at frequencies close to resonance, this trend is reversed beyond a certain SPL.

Numerical approaches [13–15] have proved to be important tools in effectively understanding the fluid dynamics involved in the interaction of a sound wave with a single-cavity single-orifice liner. Motivated by the study of Zhang et al. [14], in the present study, a simple perforated liner backed by a hexagonal cavity in grazing sound condition is considered. Simulations are performed using a Lattice-Boltzmann solver. It uses a so-called Lattice-Boltzmann Very Large Eddy Simulation (LBM-VLES) approach which is computationally less expensive when compared to DNS. This is done to avoid the geometrical simplifications necessary when performing DNS. The objective of this study is to validate the use of the LBM-VLES approach for evaluating the impedance of the liners subjected to grazing sound waves without background flow. The current study will serve as the basis for further liner investigations in the presence of a grazing laminar and turbulent boundary layer flow, which is encountered in most of the applications.

The rest of the paper is structured as follows. Section III describes the methodology with details of the numerical method, impedance eduction technique, computational domain and results of the grid refinement study. In Section IV, results of the various simulations are discussed and their comparison with both experimental measurements and previous DNS results is reported. Finally, in Section V conclusions are drawn. Supplementary results are presented in Appendix VI.

III. Methodology

A. Numerical Method

In the present study PowerFLOW 5.4b, a commercial Lattice-Boltzmann solver, is used. This is motivated by the study of Mann et al. [16] in which, it is shown that, using the LBM-VLES approach, it is possible to characterise the liners in a digital normal impedance tube setting.

The Lattice-Boltzmann method (LBM) uses the fundamental kinetic theory to determine the macroscopic fluid dynamics and the associated acoustics. In LBM, the Boltzmann equation is discretized in the velocity space to describe the evolution of the particle density distribution function. The Lattice-Boltzmann equation has the following form:

$$f_i(\mathbf{x} + c_i \Delta t, t + \Delta t) - f_i(\mathbf{x}, t) = \Omega_i(\mathbf{x}, t) \tag{11}$$

where the particle density distribution function f_i describes the probability to find a particle in an infinitesimal volume with length dx at position $\mathbf{x}$ with a discrete velocity c_i in the direction i in an infinitesimal time interval $(t, t + \Delta t)$. Further, in Eq. 11, Ω_i is the collision operator and Δ represents a small increment. In the velocity space, discrete velocity vectors are prescribed such that, at a given timestep, the distribution function can be advected from one point in

4

the mesh to N neighbouring points, including itself. For incompressible flow, a D3Q19 stencil, i.e. three dimensions and 19 discrete velocity states at each point, can be used. This configuration is shown to be sufficient to recover the Navier-Stokes equation for a perfect gas at low Mach number in isothermal conditions [17]. The collision model developed by Bhatnagar, Gross and Krook (BGK) is adopted [18]. It is expressed as:

$$\Omega_i(\mathbf{x}, t) = -\frac{\Delta t}{\tau} [f_i(\mathbf{x}, t) - f_i^{\text{eq}}(\mathbf{x}, t)] \tag{12}$$

where τ is the relaxation time and f_i^{eq} is the local equilibrium distribution function. Conventionally for low Mach number flows, a second order estimate of the Maxwell-Boltzmann equilibrium distribution function is used [17]. We have:

$$f_i^{\text{eq}}(\mathbf{x}, t) = \rho\, w_i \left[1 + \frac{c_i \mathbf{u}}{c_s^2} + \frac{(c_i \mathbf{u})^2}{2c_s^4} + \frac{|\mathbf{u}|^2}{2c_s^2} \right], \tag{13}$$

where w_i is the weight function depending on the velocity space discretisation stencil and c_s is the dimensionless speed of sound in lattice units. The non-dimensional kinematic viscosity (ν^*) is related to the relaxation time [17] by:

$$\nu^* = c_s^2 \left(\tau - \frac{\Delta t}{2} \right). \tag{14}$$

Solving Eq. 11 using an explicit time marching scheme, the hydrodynamic quantities such as density (ρ) and velocity ($\mathbf{u}$) are retrieved by summations of the moment:

$$\rho(\mathbf{x}, t) = \sum_i f_i(\mathbf{x}, t) \tag{15}$$

$$\rho\mathbf{u}(\mathbf{x}, t) = \sum_i \mathbf{c_i} f_i(\mathbf{x}, t) \tag{16}$$

The above equations, from Eq. 11 to Eq. 16 forms the general LBM scheme. At the boundaries, a algorithm based on the particle bounce-back process and the specular reflection process is implemented to replicate the no-slip and the slip conditions, respectively [19].

Solving Eq. 11 under the limits imposed by the discretisation of the velocity space and physical space is equivalent to performing DNS. However, at high Reynolds numbers, it is computationally very expensive to resolve all the length scales in the flow. Consequently, a modified version of the two equation renormalised group (RNG) k - ϵ model [20] is used to account for the unresolved sub-grid scales by adjusting the viscous relaxation time as:

$$\tau_{\text{eff}} = \tau + C_\mu \frac{k^2/\epsilon}{(1 + \eta^2)^{1/2}}, \tag{17}$$

where $C_\mu = 0.09$ and η is a combination of the local strain ($\eta_s = k|S_{ij}|/\epsilon$), local vorticity ($\eta_\omega = k|\omega_{ij}|/\epsilon$) and local helicity parameters. The term η is used to accordingly adapt the sub-grid scale viscosity in the presence of the resolved vortical structures. The implementation of the turbulence model is detailed in [21, 22]. Additionally, for wall bound flow, a modified wall model based on the generalised law-of-the-wall [23] is used. The wall model takes into account the effects of an adverse or favourable pressure gradient, and surface roughness using a length scale parameter [24]:

$$u^+ = \frac{1}{\kappa} \ln \left(\frac{y^+}{A} \right) + B \tag{18}$$

where

$$A = \begin{cases} 1 + g \left(\frac{\mathrm{d}p}{\mathrm{d}s} \frac{1}{\tau_w} \right), & \text{if } \hat{\mathbf{u}}_\tau \cdot \frac{\mathrm{d}p}{\mathrm{d}s} < 0. \\ 1, & \text{otherwise.} \end{cases}, \quad B = 5.0, \quad \kappa = 0.41, \quad y^+ = \frac{u_\tau y}{\nu}. \tag{19}$$

where u_τ and $\hat{\mathbf{u}}_\tau$, respectively, are the frictional wall velocity and its unit vector, $\frac{\mathrm{d}p}{\mathrm{d}s}$ is the pressure gradient in the streamwise direction and g is a length scale of the same order of magnitude as the unresolved near-wall region. Eq. 19 are iteratively solved to provide an estimate for the wall shear-stress in the cell closest to the wall. The so determined local skin friction in then realised using the surface collision process.

5

B. Impedance Eduction

In the present study, the two microphone approach developed by Dean [25] is used to compute the impedance. Essentially, this method involves capturing the acoustic pressure at two different microphone locations; one at the surface of the liner (p_s) and the other inside the cavity i.e., at the backplate (p_b). Fig. 2 illustrates a simplified liner showing the surface and backplate. Using these pressure data it possible to evaluate the impedance of the liner. The Dean's method assumes that the liner is locally reacting and the sound wave entering the cavity is completely reflected back, resulting in a standing wave inside the cavity.
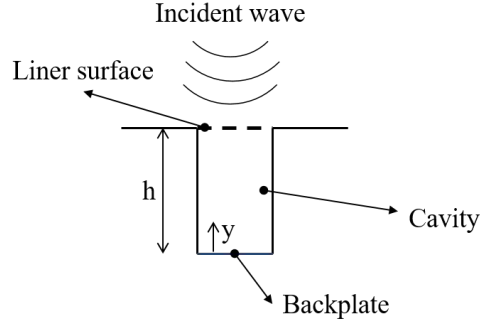

Fig. 2   Schematic of a liner showing the surface, cavity and backplate.

For an incident sound wave, $p_{inc} = p_0 e^{i(\omega t - k_a y)}$, the reflected wave will be $p_r = p_0 e^{i(\omega t + k_a y)}$. Here, $\omega = 2\pi f$, k_a is the acoustic wave number and y is the wall normal direction (see Fig. 2). The resultant standing wave inside the cavity is given by:

$$p = p_{inc} + p_r = 2p_0 e^{i\omega t} \cos(k_a y) \tag{20}$$

From the linearised momentum equation in the wall normal direction we have,

$$\frac{\partial v}{\partial t} = -\frac{1}{\rho} \frac{\partial p}{\partial y} \tag{21}$$

Differentiating Eq. 20 and integrating Eq. 21, the acoustic particle velocity (v) is obtained as:

$$v = -i \frac{2p_0}{\rho c} e^{i\omega t} \sin(k_a y) \tag{22}$$

where ρc represents the characteristic impedance of the medium. Assuming that the acoustic particle velocity normal to the surface of the liner is identical to that inside the cavity of depth (h), we have:

$$v = i \frac{2p_0}{\rho c} e^{i\omega t} \sin(k_a h) \tag{23}$$

At the backplate from Eq. 20, $p_b = 2p_0$. Since Z is defined as the ratio of the acoustic pressure to acoustic particle velocity at the surface, from Eq. 23 we have:

$$Z = \frac{p_s}{v} = -i \frac{p_s}{p_b} e^{i\phi} \operatorname{cosec}(k_a h) \tag{24}$$

where ϕ is the phase difference between the pressures p_s and p_b.

C. Computational Setup

1. Geometrical Details

The geometric model of the liner considered in the present study is a replica of the one studied by Jones et al. [26]. It consists of honeycomb cavities with a hexcell diameter of 9.5 mm and a depth of 38.1 mm. The perforated facesheet has a porosity of 6.4% and an orifice diameter of 0.99 mm. The thickness of the facesheet is 0.64 mm, which corresponds to a length-to-diameter ratio of 0.65.

6

For the initial validation study, a simplified model from Jones [26], identical to the one studied by Zhang et al. [14] is considered. The simplifications are: since the liner is locally reacting, only a single honeycomb cavity is considered; and instead of 6.4% porosity which corresponds to $6 - 7$ orifices per cavity, a single orifice at the centre of the cavity is considered. This results in a 0.99% porosity. The underlying assumption is that, the flow-fields from different orifices do not interact with each other. Fig. 3 illustrates the top and side views of the single-cavity single-orifice geometry. Henceforth, this geometry will be referred to as Config. 1.
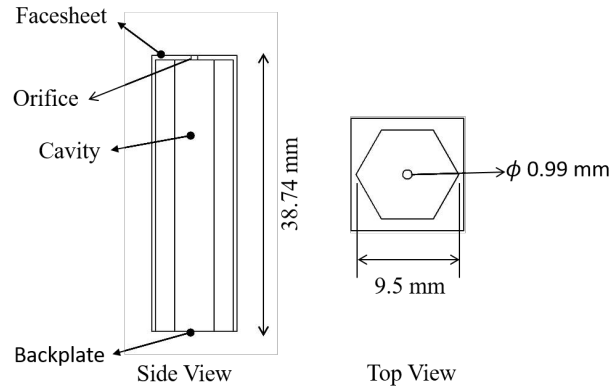

Fig. 3   Illustration of the single cavity single orifice geometry.

Then, the study is extended to a cavity with 7 orifices. Six orifices are placed at the centre of each of the six equilateral triangles that form a hexagon and one at the centre of the hexagon. This results in a porosity of 6.89% which is close to the one adopted by Jones et al. [26]. Consequently, the assumption that the flow from different orifices does not interact with each other is not required. Henceforth, this geometry will be referred to as Config. 2. Fig. 4 illustrates the difference between Config. 1 and Config. 2 geometries.
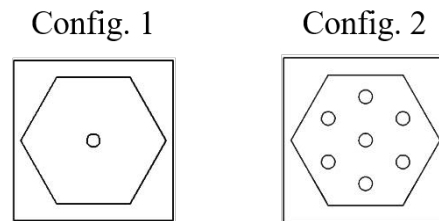

Fig. 4   Difference between Config.1 and Config. 2 geometries.

2. Computational Domain

A schematic of the computational domain is shown in Fig. 5. It consists of a duct in which the liner is placed along the top wall. The duct has two main regions defined as upstream and downstream, depending on the position of the liner and the direction of propagation of the acoustic waves. This set-up is similar to the NASA Langley Grazing Flow Impedance Tube (GFIT). The height of the duct is 63.5 mm. However in order to minimise the computational costs, the width of duct is restricted to 12 mm and periodic boundary conditions are applied on either sides. Further, no-slip and slip boundary conditions are applied at the top and bottom walls, respectively. In the upstream region, acoustic waves with a given frequency and SPL are prescribed as an initial condition. The length of the upstream region is adjusted such that it can accommodate 20 cycles/wavelengths of the acoustic wave. An appropriate Variable Resolution (VR) strategy is adapted, such that, the finest resolution cells/voxels are located in the region surrounding the orifice. The inset in Fig. 5 illustrates the grid in the vicinity of the orifice. On either sides of the upstream and the downstream regions, acoustic sponges are defined. In these sponge regions, viscosity is enhanced with a primary objective of damping or eliminating the waves originating at ends of the computational domain. The simulation time is selected such that the prescribed initial wave traverses over the surface of the liner.
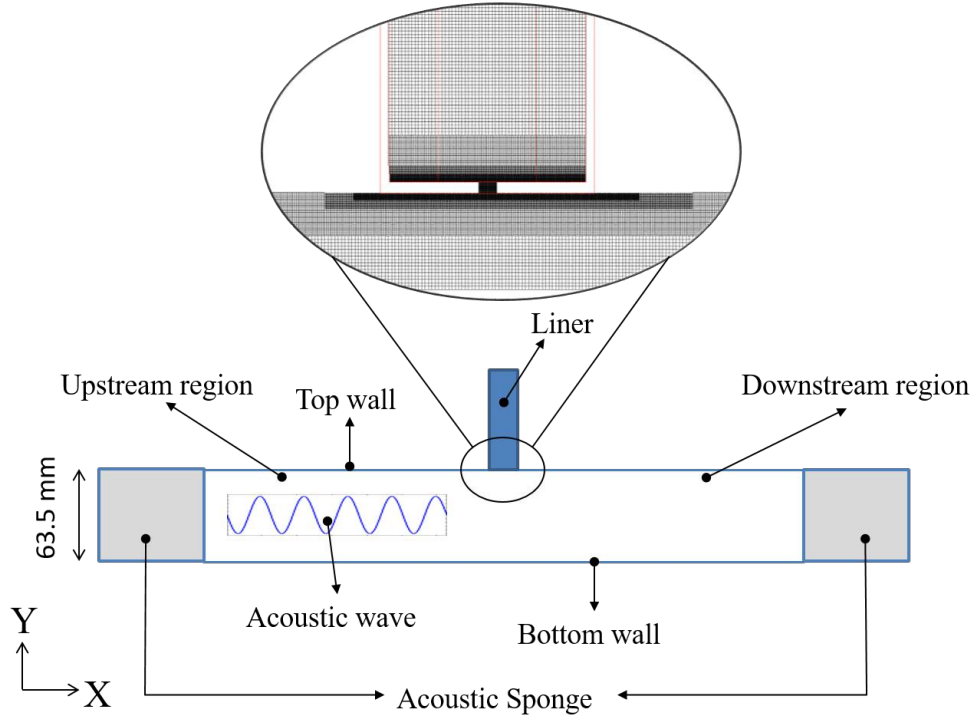
63.5 mm

Y

X

Fig. 5   Schematic of the computational domain.

The data is sampled at a frequency of 7.975 kHz. For the estimation of the impedance, data is sampled only after a statistical steady state is reached. The occurrence of this statistically steady state is found to change from one case to another, depending on the SPL and frequency of the initial acoustic excitation. The test matrix of the computations performed is shown in Table 1.

Table 1   Test matrix of the simulations.

SPL [dB]	Frequency [kHz]				
	1	1.5	2	2.5	3
120			Config. 2		
130	Config. 1	Config. 1	Config. 1 Config. 2	Config. 1	Config. 1
140			Config. 2		
150			Config. 2		
160			Config. 2		

D. Grid Refinement Study

In order to assess the influence of the grid on the flow-field and select an appropriate resolution, a grid refinement study is performed. Four grids, from now on referred to as coarse, medium, fine and very fine, are considered. The resolution of each of these grids is defined in terms of the number of voxels per orifice diameter ($N \equiv \frac{d}{\text{smallest voxel}}$). The coarse, medium, fine and very fine grids have $N = 11, 21, 42$ and 84 voxels respectively. Consequently, the grid size in terms of the number of Fine Equivalent Voxels (FEV - weighted sum of number voxels in the different VR zones) is 0.723×10^6, 2.8×10^6, 10.538×10^6 and 42.282×10^6 voxels respectively. A summary of the grid sizes and the respective computational time is reported in Table 2. For all the grids a similar VR strategy is used. Simulations are

8

performed with Config. 1 liner with grazing acoustic waves having SPL = 130 dB and f = 2 kHz .

Table 2   Summary of the differnt grids used.

Grid	Smallest Voxel	N	FEV	Total CPU-hours : Processor
Coarse	0.09375 mm	11 voxels	723997 voxels	13.07 : Xenon X5680 3.3 GHz
Medium	0.046875 mm	21 voxels	2800311 voxels	112.06 : Xenon E5-2690 2.9 GHz
Fine	0.0234375 mm	42 voxels	10538157 voxels	466.93 : Xenon E5-2697 2.6 GHz
Very fine	0.0117188 mm	84 voxels	42282616 voxels	4632 : Xenon X5680 3.3 GHz

The different grids are evaluated based on the computed resistance and reactance of the liner. In Fig. 6a and Fig. 6b the normalised resistance ($\frac{R}{\rho c_\infty}$) and normalised reactance ($\frac{X}{\rho c_\infty}$) is presented as a function of the number of voxels per orifice diameter, N and the number of FEV.
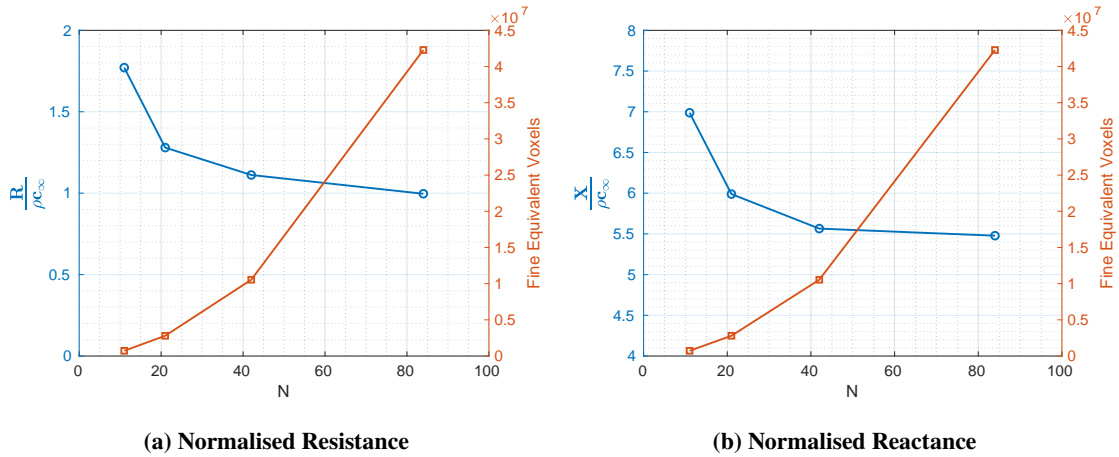

(a) Normalised Resistance

(b) Normalised Reactance

Fig. 6   Variation of impedance with the number of FEV and the number of voxels per orifice diameter (N).

The results in Fig. 6 indicate that increasing the resolution of the grid from coarse to fine, both resistance and reactance drastically reduces. The trends indicate an asymptotic behaviour of the solution. Considering the computed resistance and reactance values between the fine and very fine grid, the observed difference is small (change in resistance is 11.5% and change in reactance is 1.5%). The order of magnitude of this difference is similar to the scatter in experimental data [26] under similar initial conditions. On the other hand, for the same two grids, there is a steep increase in the FEV count (75%) and consequently, the computational cost also drastically increases. Thus, the fine grid results can be considered as a good trade-off point. Hereinafter results of all the simulations presented use the fine grid resolution.

Previously in the study of Mann et al. [16], using the same LBM-VLES approach, the grid convergence was observed with just N = 15. However a key difference in the thickness of the facesheet between the two studies is noticed. In [16], the facesheet thickness of the liner was 3 mm which is much higher than 0.64 mm of Config. 1. As a result, the number of voxels across the facesheet in Mann et al. [16] and the present study is approximately 56 and 27, respectively.

IV. Results

The results section is divided into two main sub-sections, first, the results for the liner Config. 1 are reported. This is followed by the results for the liner Config. 2. All simulations in the present study start with the acoustic waves initialised in the computational domain as previously described.

9

A. Results for geometry Config. 1

1. Instantaneous Results

The time evolution of the pressure fluctuation, $p' = p - p_\infty$, at the facesheet (away from the influence of the orifice) and at the backplate (in-line with centre of the orifice) is illustrated in Fig. 7. These results corresponds to grazing waves with SPL = 130 dB and f = 2 kHz. The associated vertical component of the velocity (v) at the centre of the orifice in the mid-plane of the facesheet is shown in Fig. 8.
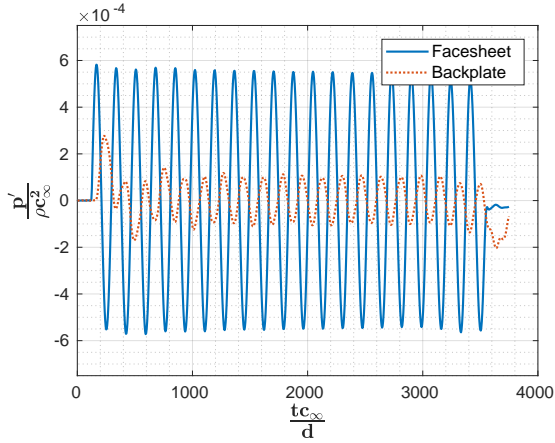

Fig. 7 Pressure fluctuations (p') at the facesheet and the backplate at SPL = 130 dB and f = 2kHz.
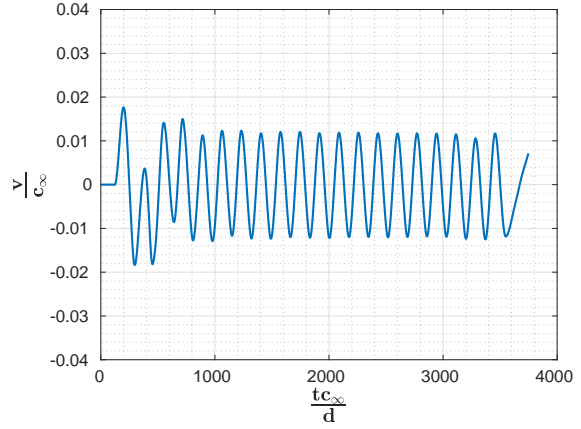
Fig. 8 Vertical component of the velocity (v) at the mid-plane of the facesheet at SPL = 130 dB and f = 2 kHz.

Both Fig. 7 and Fig. 8 show that, the sound induced flow through the orifice and inside the cavity is periodic and it reaches a statistically steady state after 8 cycles ($\frac{tc_\infty}{d} = 1400$). From Fig. 7, it is observed that the pressure fluctuation at the facesheet is much higher than the pressure fluctuation at the backplate. Changing the frequency of the acoustic waves at a constant SPL = 130 dB, changes the pressure fluctuations at the backplate [*]. Reducing the frequency, the magnitude of pressure fluctuation at the backplate is observed to increase. The vertical component of the velocity, shown in Fig. 8 for incident waves with SPL = 130 dB and f = 2 kHz, exhibits similar trends with a change in the frequency of the waves[†]. This behaviour can be further explained by considering the analytical expression for the Helmholtz resonance frequency (f_{res}) of the liner [4] given by:

$$f_{res} = \frac{c_\infty}{2\pi} \left(\frac{A}{t'_f V} \right) \tag{25}$$

where A is the orifice area, V is the volume of the cavity, t'_f is the modified neck length/facesheet thickness with $t'_f = t_f + 2\Delta t_f$ and $\Delta t_f \approx 0.8\sqrt{A/\pi}$. For Config. 1, $f_{res} \approx 723$ Hz. Thus moving closer to the resonance frequency, the pressure at the backplate and the velocity of the flow through the orifice increases. This is expected, as the maximum in pressure and velocity will occur at the resonance frequency which results in the maximum dissipation of the sound energy. At the resonance frequency, the dissipation is maximum because the conversion of the acoustic energy to the rotational energy (vortex generation) reaches the maximum. To illustrate this better, iso-surface of the λ_2 - criteria [‡] around the orifice at different frequencies at SPL= 130 dB is shown in Fig. 9. The λ_2 - criteria derived by Jeong et al. [27] is widely used to identify vortex structures. In the present context, from Fig. 9, at frequencies close to the f_{res}, a well defined vortex resembling a vortex ring is observed. The same can not be said about the higher frequencies as the vortices are observed to be confined to a region in the proximity of the orifice.

The above-described trends for pressure fluctuations, velocity and vortex structure, are very similar to those previously reported in Zhang et al. [14].

---

[*]Results for variation of pressure fluctuations with frequencies for Config.1 are shown in Fig. 19, Appendix VI

[†]Results for variation of vertical component of velocity with frequencies for Config.1 is shown in Fig. 20, Appendix VI

[‡]The threshold of λ_2 criteria is set to -5×10^6

10

(a) f = 1 kHz   **(b)** f = 1.5 kHz   **(c)** f = 2 kHz

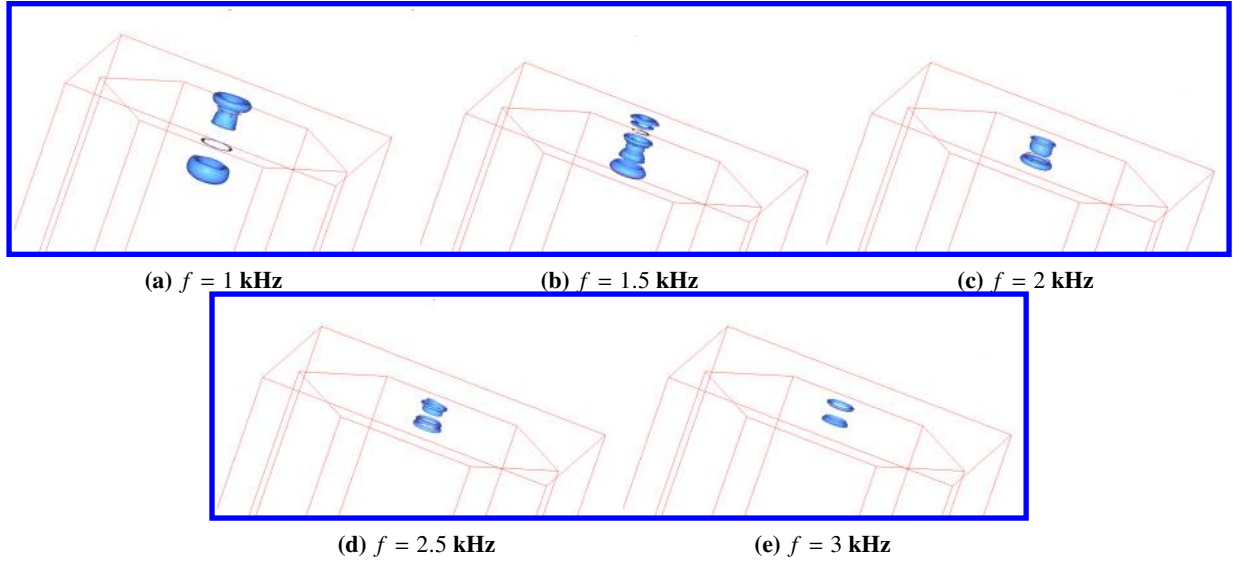**(d)** f = 2.5 kHz   **(e)** f = 3 kHz

Fig. 9 λ_2 **iso-surfaces of the induced flow-field around the orifice at different frequencies of the grazing waves with SPL = 130 dB.**

2. Phase Averaged Results

To gain further insight into the periodic nature of the sound induced flow-field, phase averaged results are examined. Four phases, $\phi = 0, \frac{\pi}{2}, \pi$ and $\frac{3\pi}{2}$ are considered. The phase, $\phi = 0$ corresponds to a maximum in the vertical component of the velocity, representing an inward flow (i.e., flow entering the cavity). The phase, $\phi = \pi$ corresponds to a minimum in the vertical component of the velocity, representing an outward flow (i.e., flow out of the cavity). On the other hand, phases $\phi = \frac{\pi}{2}$ and $\frac{3\pi}{2}$ represents a change in the direction of the flow through the orifice, inward-to-outward and outward-to-inward, respectively.

The phase-averaged vertical component of the velocity ($< v >$) at the mid-plane of the facesheet for different frequencies at SPL = 130 dB is shown in Fig. 10. Individually, these velocity profiles can be split into two different regions: the core region and the boundary layer region. The boundary layer region is associated with a steep gradient in the velocity profile. These are observed at the ends of the orifice. The region in the middle, which is comparatively more uniform, is the core region. An illustration of the boundary layer regions (BL region) and the core region for f = 1 kHz and $\phi = 0$ is shown in Fig. 10a. With a change in frequency, Fig. 10 shows that $< v >$ is maximum at the frequency closest to the resonance frequency. Correspondingly, the BL regions also increases near the resonance frequency. On the other hand, the core region is less uniform near the resonance frequency. This non-uniform flow is most likely due to the influence of the strong vortex ring observed close to the resonance frequency.

3. Impedance Results

To further validate the use of LBM-VLES approach, the computed impedance values for the liner are compared with the experimental results reported in Jones et al. [26] and the DNS results from Zhang et al. [14]. In order to compute the impedance, the in-situ method previously described in Section B is used. For Config. 1, pressure data on the surface (p_s) is acquired at 120 points distributed in concentric circles around the orifice. The circles start at radius, $r_c = d$ and extend up-till $r_c = 5d$ in steps of $0.5d$. An illustration of these data points is shown in Fig. 11. For the pressure at the backplate (p_b), the point aligned with the centre of the orifice is selected. The averaged value of impedance which is normalised by ρc_∞ and multiplied by the porosity for different frequencies at SPL= 130 dB is shown in Fig. 12. The real part of impedance, $\theta\sigma$ ($\theta \equiv \frac{R}{\rho c_\infty}$) is shown in Figs. 12a, 12c and the imaginary part $\chi\sigma$ ($\chi \equiv \frac{X}{\rho c_\infty}$) in Figs. 12b, 12d. Results from the current simulation are abbreviated as 'Sim', and the length of the error bar corresponds to the standard deviation of the computed values.

Following Melling [7], for a liner in the linear regime, if the orifices are symmetrically placed and there is no interaction between the induced flow through the orifices, then $Z\sigma$ can be assumed to be independent of porosity. However in Fig. 12, for the experimental results (stars and circles) from [26], the normalised resistance and reactance of the liners with $\sigma = 6.4\%$ and 15% do not collapse on each other when multiplied by its respective porosities. This
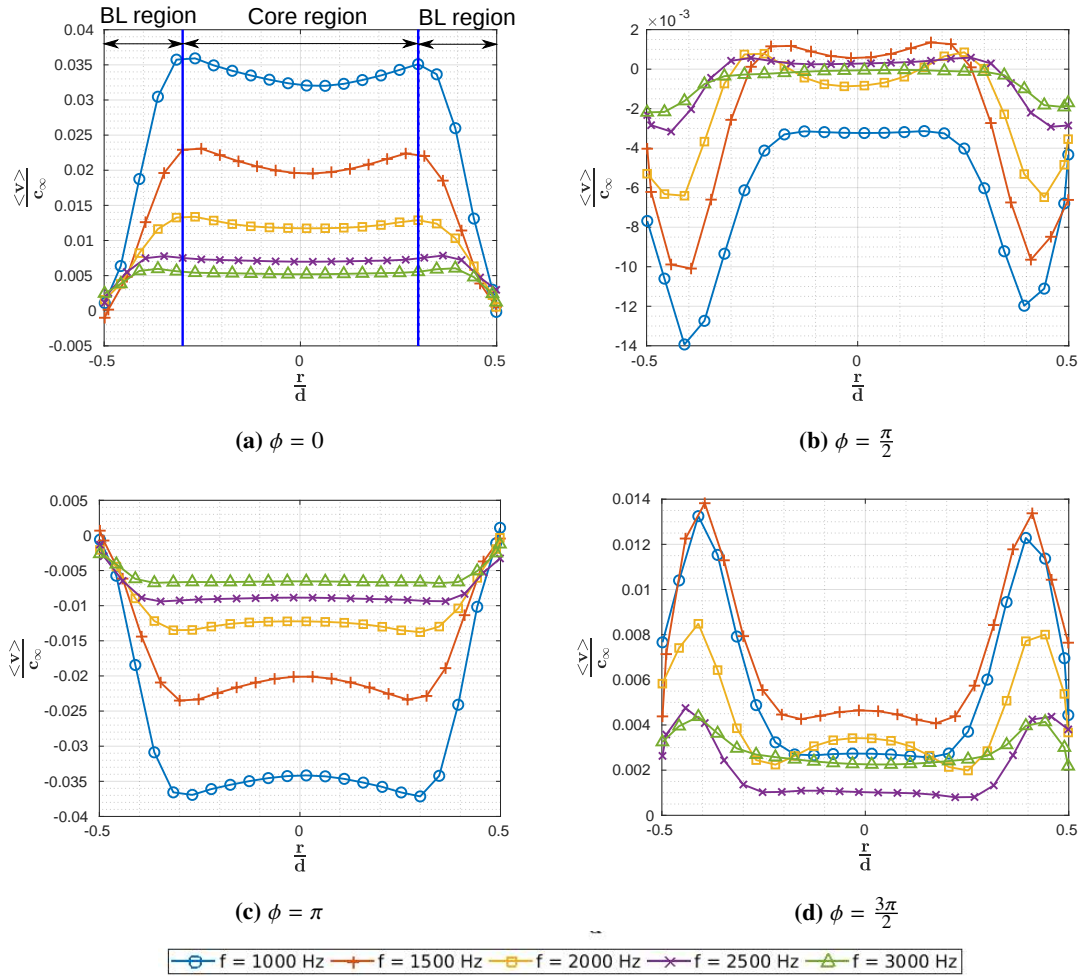
11

(a) $\phi = 0$

(b) $\phi = \frac{\pi}{2}$

(c) $\phi = \pi$

(d) $\phi = \frac{3\pi}{2}$

f = 1000 Hz   f = 1500 Hz   f = 2000 Hz   f = 2500 Hz   f = 3000 Hz

Fig. 10   Phase averaged velocity ($< v >$) at the mid-plane of the orifice for different frequencies of the grazing waves with SPL $= 130$ dB.

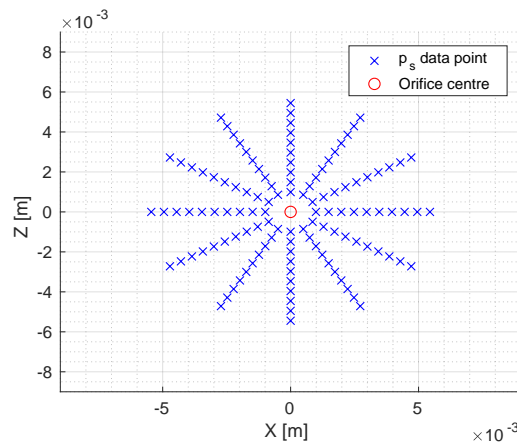**Fig. 11   Illustration of the surface pressure (p_s) data points for Config. 1.**

12

(a) Resistance

(b) Reactance

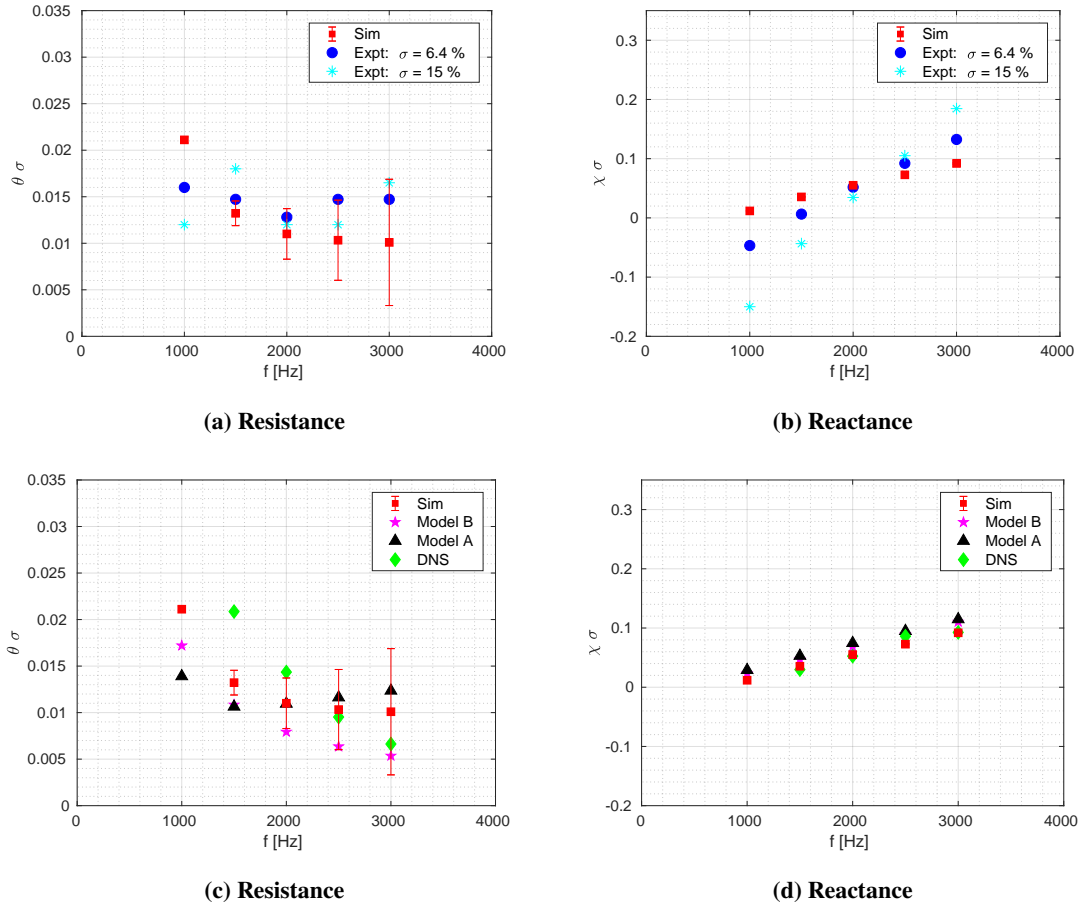**(c) Resistance**

(d) Reactance

Fig. 12   Comparison of predicted resistance and reactance for Config. 1 at different frequencies of the grazing waves with SPL = 130 dB. Legends: Model A - Melling's model; Model B - Motsinger's model.

suggests that, some of the conditions necessary for porosity independent $Z\sigma$ might not be satisfied. Nonetheless, comparing the experimental results with the simulation results in Fig 12a, it is seen that the results are similar. Deviations are observed at the highest and the lowest frequencies considered. At the lowest frequency, the difference is most likely due to the difference in the resonance frequency of the compared liners. This is evident in Fig. 12b, where the $\chi\sigma$ curves for the liners crosses the zero line at different frequencies. As a matter of fact, at resonance reactance is zero. On the other hand, the reason for deviation at the highest frequency is not clear.

Comparing the simulation results with the DNS results from [14] in Fig. 12c, the $\theta\sigma$ values are in agreement at $f = 2$ and 2.5 kHz but, at $f = 1.5$ and 2.5 kHz results from the current simulations are seen to be in better agreement with the experimental values. At this stage, it is important to note that, in [14] the acoustic waves are incident normal to the surface of the liner while in the present study, acoustic waves are grazing over the surface of the liner. On the other hand, the computed reactance in Fig. 12d is in very good agreement with the DNS results.

Comparing the resistance from the simulations with the corresponding predictions from the analytical models described in Section II, the trends are in better agreement with Melling's model. It is to be noted that, for the impedance predictions using the analytical models, a $C_D = 0.76$, recommended in Motsinger et al. [3] is used. However, C_D is expected to change with the Reynolds number of the flow through the orifice [7]. This in turn could be responsible for some of the observed differences between the simulated and analytical results. The reactance in Fig. 12d shows a very good agreement with the predictions from the models, with less than 3% difference observed at all the frequencies. The difference in predictions from Melling's model and Motsinger's model is negligible.

From the above-discussed results for liner geometry Config. 1, it can be said that using the LBM-VLES approach it is possible to solve the different mechanism responsible for dissipation of incident sound wave.

13

B. Results for geometry Config. 2

1. Instantaneous Results

The time evolution of the pressure and the velocity fluctuations, for the orifice at the centre of the cavity is shown in Fig 13 and Fig. 14, respectively. These results corresponds to grazing waves with SPL = 130 dB and f = 2 kHz. Fig. 13 shows that, the amplitude of the pressure fluctuation at the backplate is much higher than the one at the facesheet. As a result, the ratio of pressure fluctuations is less than 1. This observation is not valid with an increase in the SPL of the grazing waves. This is because, as the liner enters the non-linear regime, the ratio of pressure fluctuation increases [§]. At the highest SPL (160 dB) considered, the pressure fluctuation ratio is greater than 1. Furthermore, at SPL = 150 dB and above, deviations from the sinusoidal nature of the pressure fluctuations at the backplate is observed. These deviations are indicative of the non-linear behaviour and are consistent with the observations in Zhang et al. [14].
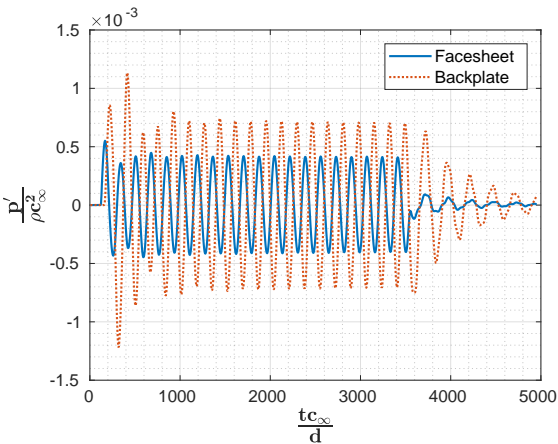

Fig. 13 Pressure fluctuations (p') at the facesheet and the backplate at SPL = 130 dB and f = 2 kHz.
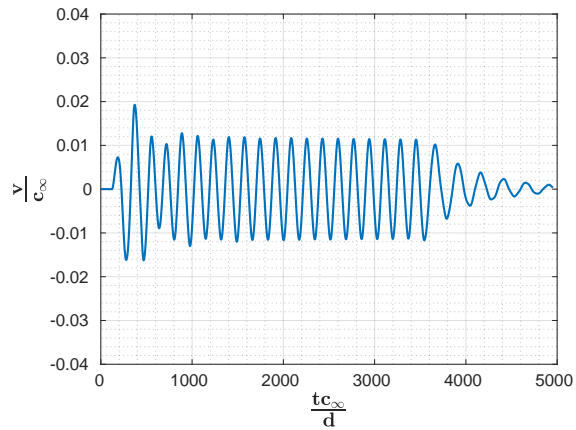
Fig. 14 Vertical component of the velocity (v) at the mid-plane of facesheet at f = 2 kHz and SPL = 130 dB.

The vertical component of the velocity (v) for both, Config. 2 and Config. 1 shown in Fig. 14 and Fig. 8, respectively, are similar for acoustic excitations with SPL = 130 dB and f = 2 kHz. Thus suggesting that, there is no interaction between the flow-fields from the different orifices. Additionally, with an increase in the SPL of the grazing waves, the vertical component of the velocity also increases [¶]. The deviations from sinusoidal behaviour are visible only at SPL = 160 dB.

The iso-surfaces of the λ_2 - criteria for Config. 2 liner are illustrated in Fig. 15. The iso-surfaces are coloured by the magnitude of static pressure to distinguish between the vortex structures inside and outside of the cavity. The threshold of λ_2 is set at -5×10^7 for all cases expect at SPL = 160 dB, for which a threshold of -5×10^8 is used to improve visibility.

Fig. 15 shows that the presence of the dominant vortex structures increases with an increase in the SPL of the grazing waves. Starting from a SPL of 130 dB, the presence of coherent vortex rings is observed. Interestingly, at SPL = 140 dB, the presence of secondary structures, encompassing the primary rings, is also observed. In Archer et al. [28] it is highlighted that the generation of secondary structures coincides with the deformation of the primary rings, resulting in the transition of the vortex rings from a laminar state to a turbulent state. The vortex ring is considered to be fully turbulent when the secondary structure is shed into hairpin vortices [28]. In Fig. 21, it was observed that the indicators of non-linear behaviour are visible starting from SPL = 150 dB. However, from Fig. 15, because of the observed vortex ring transition, it is possible to expect some non-linear behaviour at SPL = 140 dB. Further, at SPL = 150 dB, the presence of numerous hairpin structures are visible, suggesting a fully turbulent behaviour. These structures are found to be further enhanced at SPL = 160 dB.

[§]Results for the variation of pressure fluctuations with SPL are presented in the Appendix section, Fig. 21

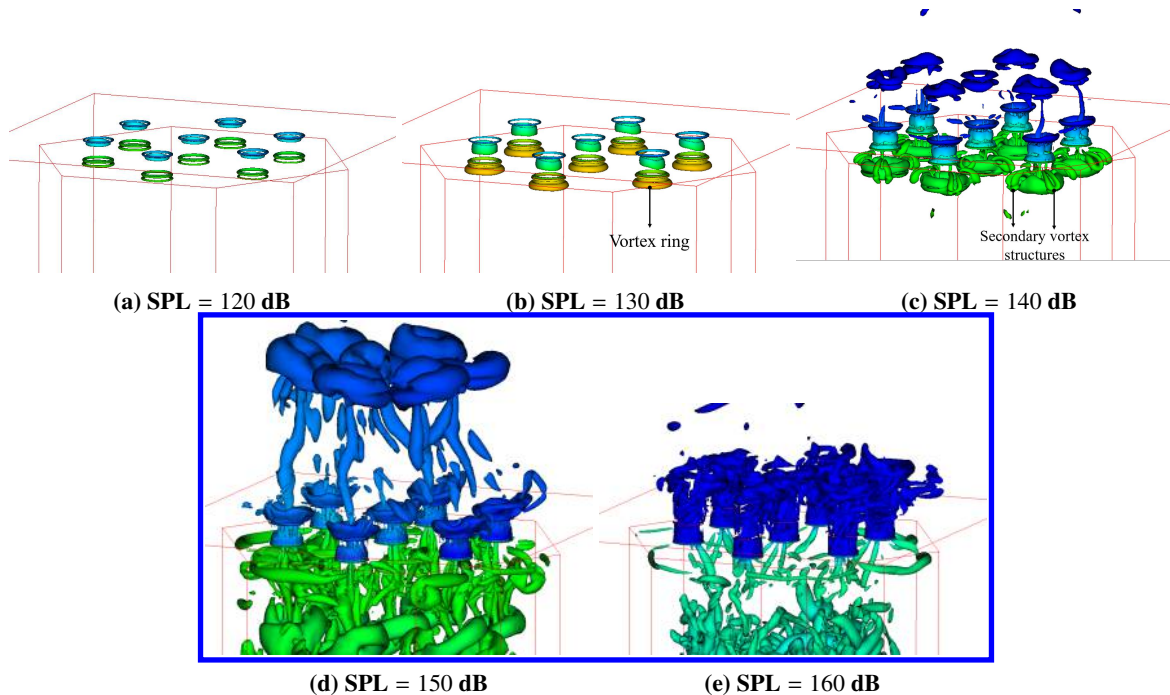[¶]Results for the variation in v with a change in SPL are presented in the Appendix section, Fig. 22

14

(a) SPL = 120 **dB**   **(b) SPL** = 130 **dB**   **(c) SPL** = 140 **dB**

(d) SPL = 150 **dB**   **(e) SPL** = 160 **dB**

Fig. 15 λ_2 **iso-surfaces of the induced flow-fields at different SPLs of the grazing waves with** f = 2 **kHz.**

2. Phase Averaged Results

The phase-averaged vertical component of the velocity ($< v >$) in the mid-plane of the facesheet for phases, $\phi = 0, \frac{\pi}{2}, \pi$ and $\frac{3\pi}{2}$ with a change in SPL of the grazing waves is shown in Fig. 16.

Fig. 16 shows that, increasing the SPL of the grazing waves results in an increase in the boundary layer region of the induced flow-fields. Additionally, the velocity profiles at the different phases are observed to deviate from one another in accordance with the dominant flow features. At SPL = 120 dB, from previous results, no dominant vortex structures are observed. Consequently, the velocity profiles are observed to be flat in the core region. However, at SPL = 130 dB, the presence of a coherent laminar vortex ring was observed and as a result, a wavy pattern is observed in the core region (see Fig.16c and Fig. 16d).

The phase averaged results for both, Config. 1 and Config. 2 shown in Fig. 10 and Fig. 16, respectively, are similar for grazing waves with SPL = 130 dB and f = 2 kHz. The presence of a wavy core region is evident in both the cases. Thereby showing that at SPL = 130 dB for Config. 2, it is unlikely that the induced flow-fields through the different orifices are interacting.

3. Impedance Results

The characteristic impedance of the Config. 2 liner is also calculated using the in-situ technique previously described. For Config. 2, the pressure data on the surface (p_s) for each of the orifice is acquired at 12 points encircling the orifice with a radius d. An illustration of these data points is shown in Fig. 17. For the pressure data at the backplate (p_b), the points aligned with the centre of the respective orifices is selected. Fig. 18 illustrates the evolution of the average value of the computed impedance with a change in the SPL of the grazing waves with f = 2 kHz. The real and imaginary parts of the impedance are normalised by ρc_∞ and plotted in Fig. 18a and Fig. 18b, respectively.

In Jones et al. [26] for a liner similar to Config. 2, with porosity 6.4%, the experimental results for impedance using three different set-ups, namely, normal incidence tube (NIT) and two different versions of the grazing impedance tube, GIT-TB and GIT-95M are reported. Comparing the results from the current simulation (labelled as 'Sim') at SPL = 130 dB and f = 2 kHz with the corresponding experimental results, it is observed that, the resistance is in good agreement. The predicted value of resistance lies within the experimental scatter. On the other hand, reactance is observed to be under predicted with respect to the experimental NIT results, but its value is close to the values from GIT-TB and GIT-95M set-ups. This is because, the initial conditions in the simulations are very similar to those in GIT-TB and
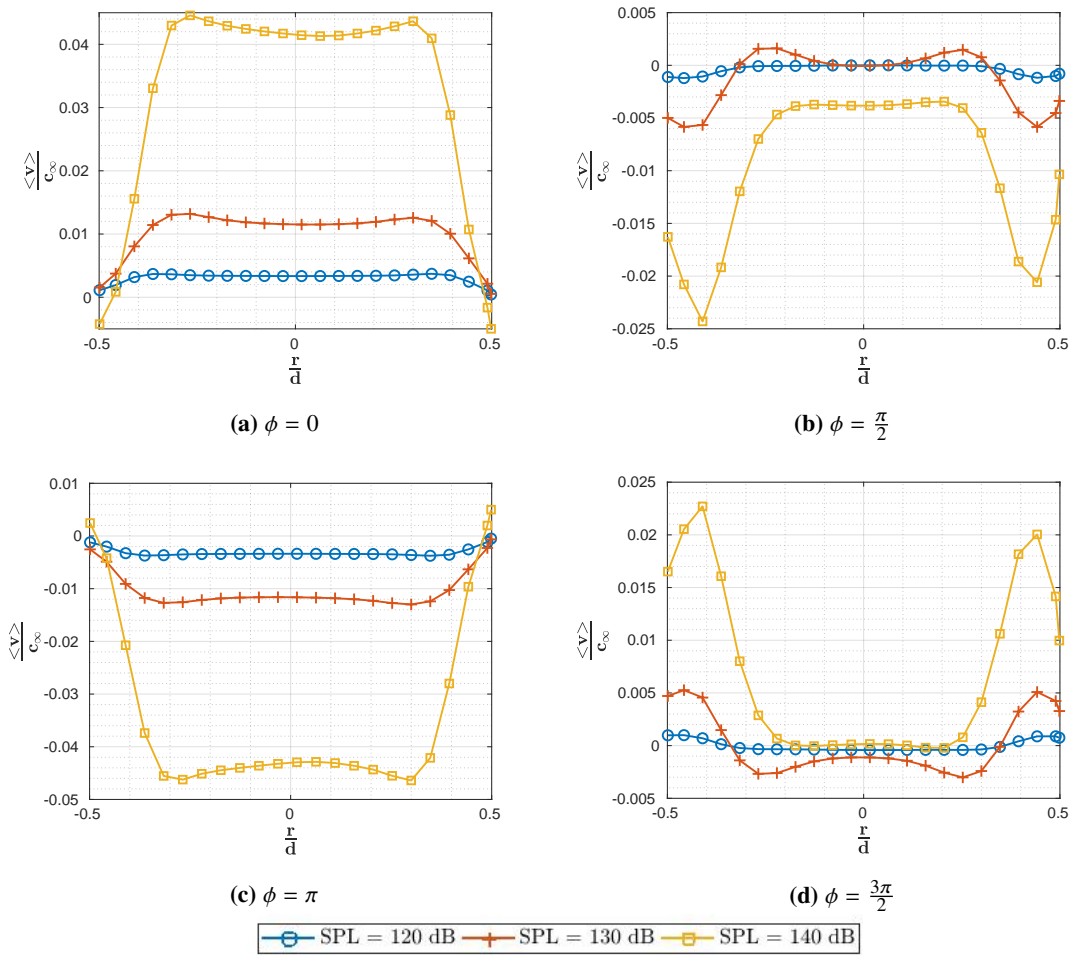
15

(a) $\phi = 0$

(b) $\phi = \frac{\pi}{2}$

(c) $\phi = \pi$

(d) $\phi = \frac{3\pi}{2}$

SPL = 120 dB   SPL = 130 dB   SPL = 140 dB

Fig. 16 **Phase averaged velocity (<v>) at the mid-plane of the orifice with change in SPL of the grazing waves at $f = 2$ kHz.**
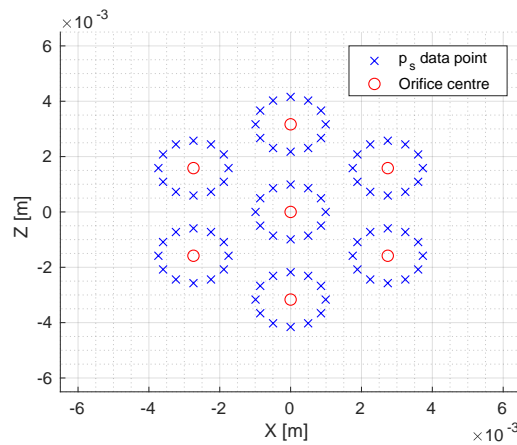

Fig. 17 **Illustration of the surface pressure (p_s) data points for Config. 2.**

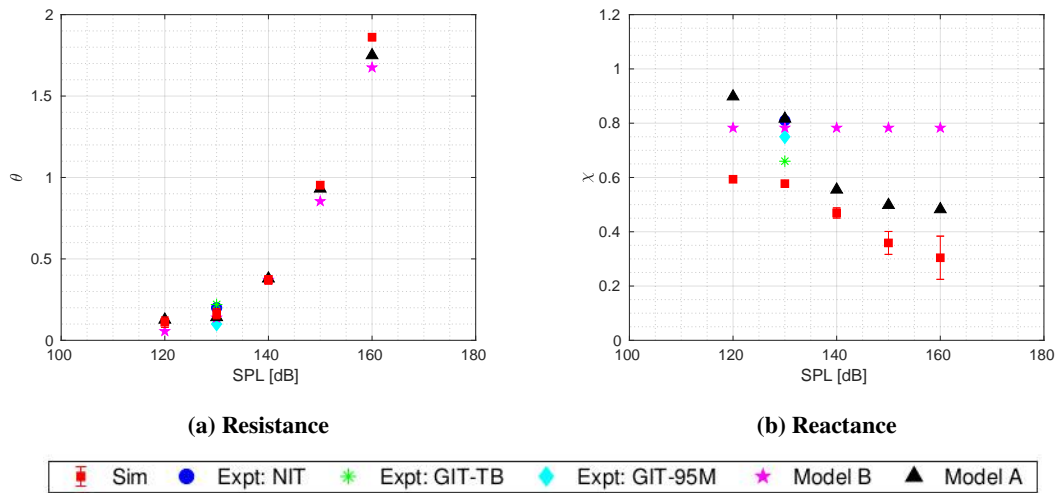**Fig. 18   Comparison of the predicted resistance and reactance for Config. 2 at different SPLs of the grazing waves at f = 2 kHz. Legends: Model A - Melling's model; Model B - Motsinger's model.**

GIT-95M. A possible explanation for this drop in reactance could be due to the reduction in the mass reactance in the presence of grazing sound waves. However a more detailed analysis will be necessary to clearly establish this aspect. The comparison of impedance values is reported in Table 3.

Table 3   Comparison of impedance results for SPL = 130 dB at f = 2 kHz.

	NIT	GIT-TB	GIT-95M	Sim
θ	0.2	0.22	0.10	0.1636
χ	0.81	0.66	0.75	0.5773

Fig. 18a shows that, with an increase in the SPL of the grazing waves, the resistance increases rapidly. This increase coincides with the observed shedding of the coherent vortex rings and its transition to a turbulent state. On the other hand in Fig. 18b, reactance is observed to decrease with an increase in the SPL. These trends are seen to be consistent with the DNS results in Roche et al. [15] and Tam et al. [29]. Further, comparing the simulation results for the resistance in Fig. 18a with the predictions from the analytical models (both, Melling's model and Motsinger's model), a good agreement, except at very high SPL = 160 dB, is observed. From Fig 18b, reactance is observed to be over-predicted by the analytical models. This deviation could be due to the fact that analytical models are derived with an assumption of normal sound incidence and in the present study, a constant value of C_D is used for the analytical predictions. However qualitatively, the results from Melling's model are observed to be consistent with the simulations. In case of the predictions from Motsinger's model, as Eq. 8 is not dependent on the intensity of the incident waves, the reactance remains constant.

V. Conclusion

Using LBM-VLES approach in conjunction with the in-situ method, the impedance of the acoustic liner is successfully predicted for grazing sound without flow. Two geometries, one, with a single orifice corresponding to 0.99% porosity identical to Zhang et al.[14] and the other with 6.89% porosity, are considered. The first geometry is a simplified model from Jones et al. [26] with an underlying assumption that induced flow-fields from different orifices do not interact with each other. This liner is subjected to grazing acoustic waves with frequency varying from 1 kHz to 3 kHz at a constant SPL of 130 dB. The results from these simulations are in general agreement with the reference [14], thereby validating the computational set-up. The second geometry with 6.89% porosity is similar to the model adopted by Jones et al. [26] and the assumption about the induced flow-fields is no longer necessary. This liner is subjected to grazing acoustic

waves with SPL varying from 120 dB to 160 dB at a constant frequency of 2 kHz. Results from the simulation show that for the considered liner geometry at SPL = 130 dB and f = 2 kHz, no notable influence of the orifices interactions are observed. With a change in SPL of the incident acoustic wave, the transition of the shed vortex ring from a laminar state to turbulent state with the occurrence of secondary structures is observed at SPL = 140 dB. Resistance is observed to increase rapidly, coinciding with the transition of the vortex rings. On the other hand, reactance is observed to reduce. These results are observed to be consistent with the predictions from semi-empirical models by Melling [7].

The present study illustrates the ability of the LBM-VLES approach to effectively characterise the performance of the liners without geometrical simplifications and investigate the flow physics. Looking ahead, as a natural extension of the current work, the presence of a boundary layer flow and its influence on the characteristics of the liner will be investigated. A key challenge will be to isolate the hydrodynamic and acoustic pressure fluctuations which will be necessary to predict the impedance accurately.

Acknowledgements

VI. Appendix

A. Additional Results

(a) $f = 1$ **kHz**

(b) $f = 1.5$ **kHz**

(c) $f = 2.5$ **kHz**

(d) $f = 3$ **kHz**

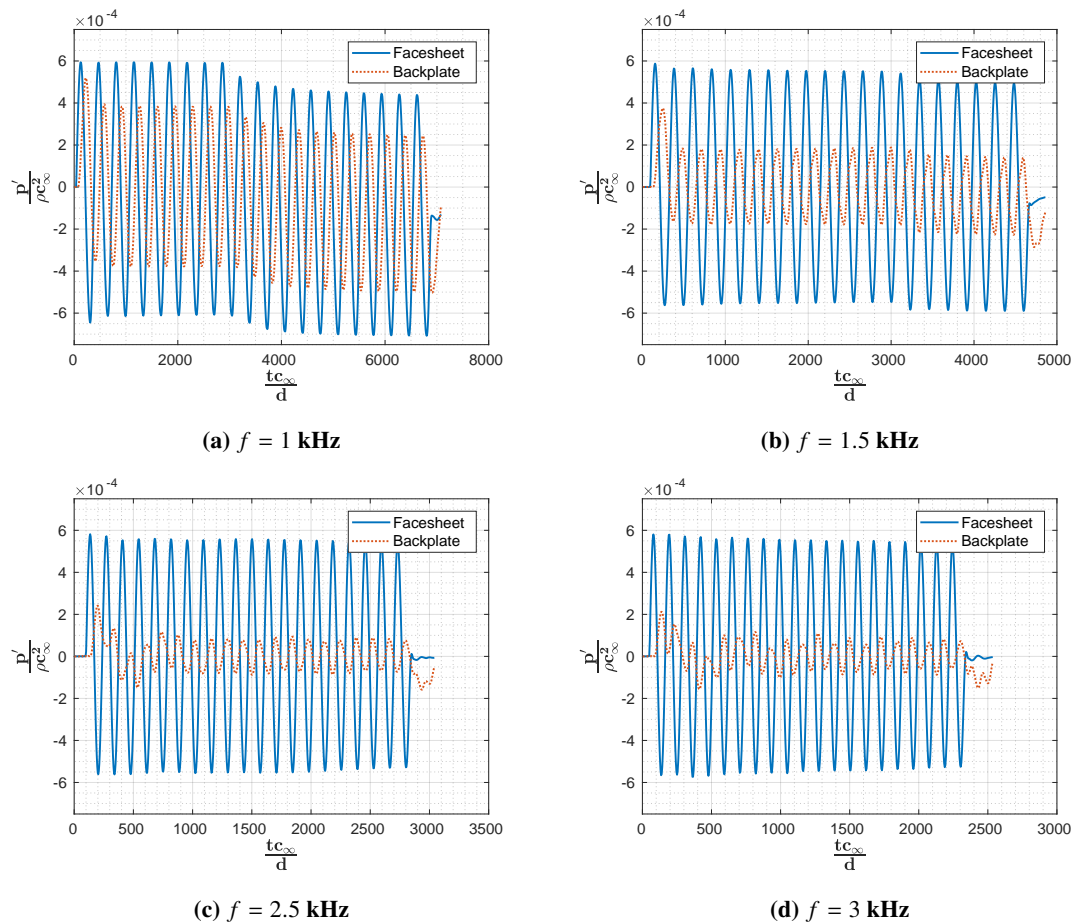**Fig. 19 Pressure fluctuations (p') at the facesheet and the backplate at different frequencies of the grazing waves with SPL = 130 dB**

19

(a) f = 1 kHz

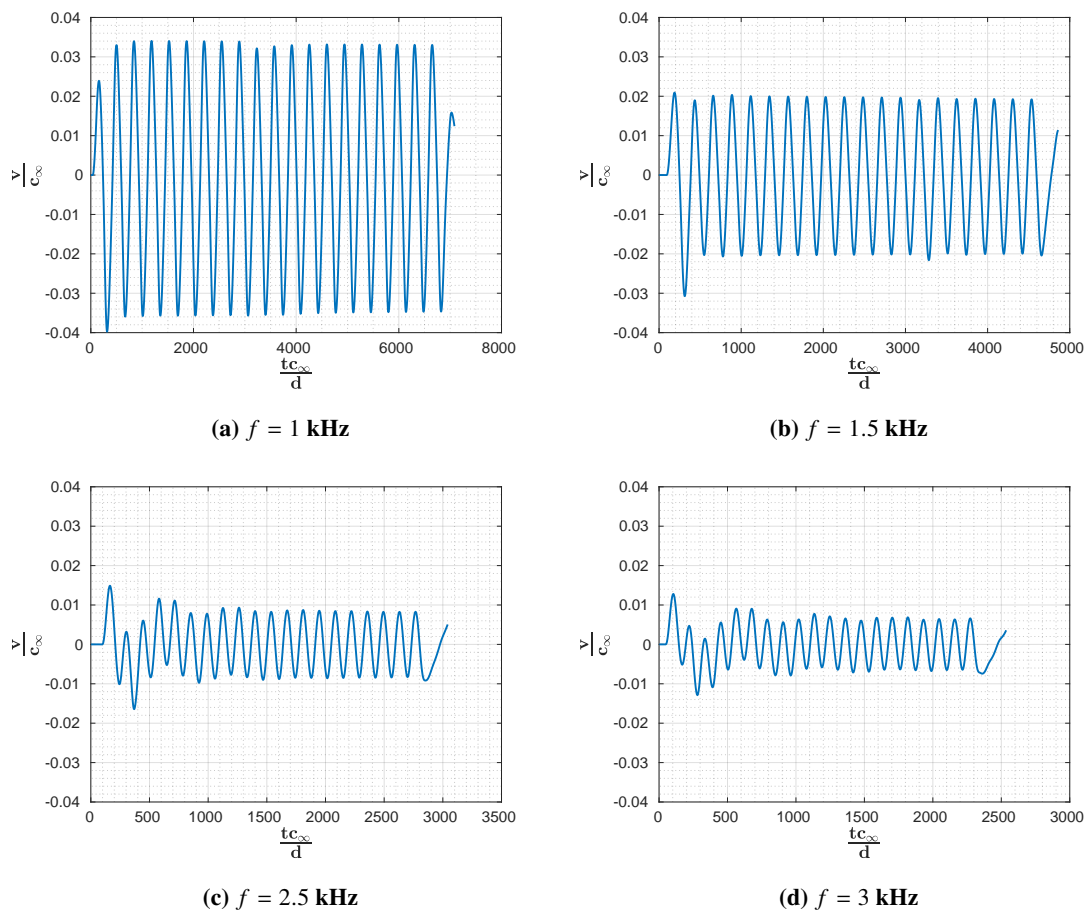**(b)** f = 1.5 kHz

(c) f = 2.5 kHz

(d) f = 3 kHz

Fig. 20   The vertical component of the velocity (v) at the mid-plane of facesheet at different frequencies of the grazing waves with SPL = 130 dB.
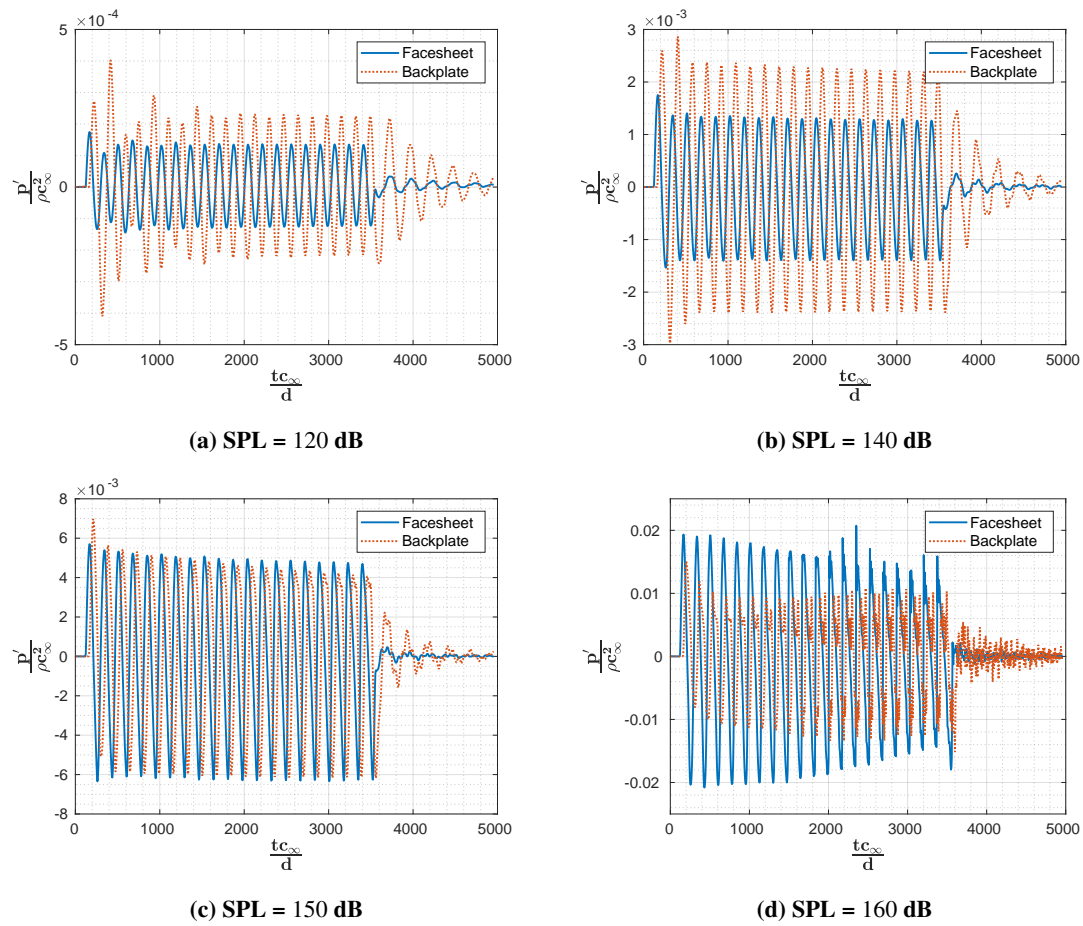
(a) SPL = 120 dB

(b) SPL = 140 dB

(c) SPL = 150 dB

(d) SPL = 160 dB

Fig. 21   Pressure fluctuations (p') at the facesheet and the backplate at different SPL of the grazing waves with $f = 2$ kHz.

(a) SPL = 120 dB

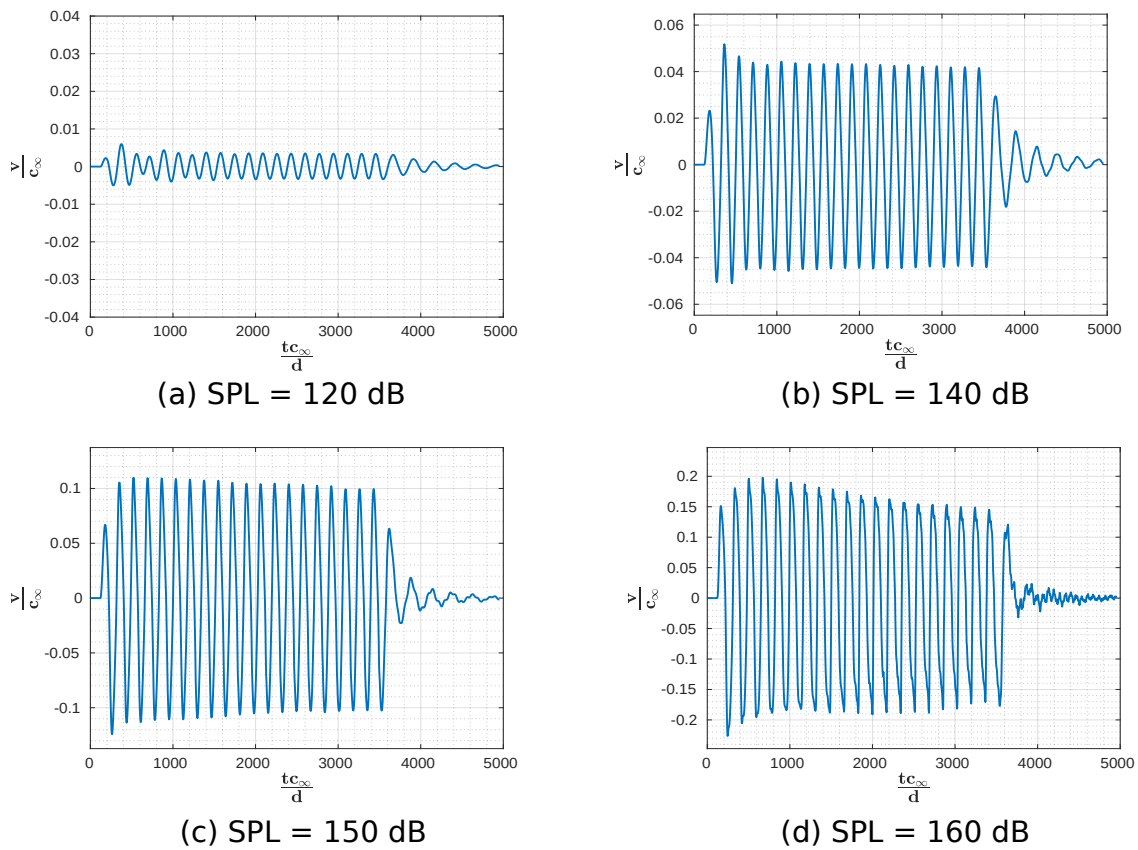(b) SPL = 140 dB

(c) SPL = 150 dB

(d) SPL = 160 dB

Fig. 22 The vertical component of the velocity (v) at the mid-plane of the facesheet at different SPL of the grazing waves with $f = 2$ kHz.

References

[1] Bureau, I. A. T., "Aircraft Noise Technology and International Noise Standards," 2014.

[2] Low, J. K., "Ultra-high bypass ratio jet noise," 1994.

[3] Motsinger, R., and Kraft, R., "Design and performance of duct acoustic treatment," 1991.

[4] Zhang, Q., and Bodony, D. J., "Numerical investigation of a honeycomb liner grazed by laminar and turbulent boundary layers," *Journal of Fluid Mechanics*, Vol. 792, 2016, pp. 936–980.

[5] Sivian, L., "Acoustic impedance of small orifices," *The Journal of the Acoustical Society of America*, Vol. 7, No. 2, 1935, pp. 94–101.

[6] Ingård, U., and Labate, S., "Acoustic circulation effects and the nonlinear impedance of orifices," *The Journal of the Acoustical Society of America*, Vol. 22, No. 2, 1950, pp. 211–218.

[7] Melling, T. H., "The acoustic impendance of perforates at medium and high sound pressure levels," *Journal of Sound and Vibration*, Vol. 29, No. 1, 1973, pp. 1–65.

[8] Rogers, T., and Hersh, A., "The effect of grazing flow on the steady state resistance of square-edged orifices," *AEROACOUSTICS: FAN NOISE AND CONTROL; DUCT ACOUSTICS; ROTOR NOISE*, Vol. 43, 1976.

[9] Howe, M., "A note on the interaction of unsteady flow with an acoustic liner," *Journal of Sound and Vibration*, Vol. 63, No. 3, 1979, pp. 429–436.

[10] Crandall, I. B., *Theory of vibrating systems and sound*, D. Van Nostrand Company, 1954.

[11] Kraft, R., Yu, J., and Kwan, H., "Acoustic Treatment Design Scaling Methods. Volume 2; Advanced Treatment Impedance Models for High Frequency Ranges," 1999.

[12] W. Tam, C. K., and Kurbatskii, K. A., "Microfluid dynamics and acoustics of resonant liners," *AIAA journal*, Vol. 38, No. 8, 2000, pp. 1331–1339.

[13] Tam, C. K., Kurbatskii, K. A., Ahuja, K., and Gaeta Jr, R., "A numerical and experimental investigation of the dissipation mechanisms of resonant acoustic liners," *Journal of Sound and Vibration*, Vol. 245, No. 3, 2001, pp. 545–557.

[14] Zhang, Q., and Bodony, D. J., "Numerical investigation and modelling of acoustically excited flow through a circular orifice backed by a hexagonal cavity," *Journal of Fluid Mechanics*, Vol. 693, 2012, pp. 367–401.

[15] Roche, J.-M., Leylekian, L., Delattre, G., and Vuillot, F., "Aircraft fan noise absorption: DNS of the acoustic dissipation of resonant liners," *15th AIAA/CEAS Aeroacoustics Conference (30th AIAA Aeroacoustics Conference)*, 2009, p. 3146.

[16] Mann, A., Pérot, F., Kim, M.-S., and Casalino, D., "Characterization of acoustic liners absorption using a Lattice-Boltzmann method," *Proceeding of the 19th AIAA-CEAS Aeroacoustics Conference*, 2013.

[17] Chen, H., Chen, S., and Matthaeus, W. H., "Recovery of the Navier-Stokes equations using a lattice-gas Boltzmann method," *Physical Review A*, Vol. 45, No. 8, 1992, p. R5339.

[18] Bhatnagar, P. L., Gross, E. P., and Krook, M., "A model for collision processes in gases. I. Small amplitude processes in charged and neutral one-component systems," *Physical review*, Vol. 94, No. 3, 1954, p. 511.

[19] Chen, H., Teixeira, C., and Molvig, K., "Realization of fluid boundary conditions via discrete Boltzmann dynamics," *International Journal of Modern Physics C*, Vol. 9, No. 08, 1998, pp. 1281–1292.

[20] Yakhot, V., and Orszag, S. A., "Renormalization group analysis of turbulence. I. Basic theory," *Journal of scientific computing*, Vol. 1, No. 1, 1986, pp. 3–51.

[21] Chen, H., Orszag, S. A., Staroselsky, I., and Succi, S., "Expanded analogy between Boltzmann kinetic theory of fluids and turbulence," *Journal of Fluid Mechanics*, Vol. 519, 2004, pp. 301–314.

[22] Chen, H., Kandasamy, S., Orszag, S., Shock, R., Succi, S., and Yakhot, V., "Extended Boltzmann kinetic equation for turbulent flows," *Science*, Vol. 301, No. 5633, 2003, pp. 633–636.

[23] Launder, B. E., and Spalding, D. B., "The numerical computation of turbulent flows," *Numerical Prediction of Flow, Heat Transfer, Turbulence and Combustion*, Elsevier, 1983, pp. 96–116.

[24] Anagnost, A., Alajbegovic, A., Chen, H., Hill, D., Teixeira, C., and Molvig, K., "DIGITAL PHYSICS™ Analysis of the Morel Body in Ground Proximity," Tech. rep., SAE Technical Paper, 1997.

[25] Dean, P., "An in situ method of wall acoustic impedance measurement in flow ducts," *Journal of Sound and Vibration*, Vol. 34, No. 1, 1974, pp. 97–IN6.

[26] Jones, M., Watson, W., Parrott, T., and Smith, C., "Design and evaluation of modifications to the NASA Langley flow impedance tube," *10th AIAA/CEAS Aeroacoustics Conference*, 2004, p. 2837.

[27] Jeong, J., and Hussain, F., "On the identification of a vortex," *Journal of fluid mechanics*, Vol. 285, 1995, pp. 69–94.

[28] Archer, P., Thomas, T., and Coleman, G., "Direct numerical simulation of vortex ring evolution from the laminar to the early turbulent regime," *Journal of Fluid Mechanics*, Vol. 598, 2008, pp. 201–226.

[29] Tam, C. K., Ju, H., Jones, M. G., Watson, W. R., and Parrott, T. L., "A computational and experimental study of resonators in three dimensions," *Journal of Sound and Vibration*, Vol. 329, No. 24, 2010, pp. 5164–5193.

This article has been cited by:

1. Francesco Avallone, Casalino Damiano. Acoustic-induced velocity in a multi-orifice acoustic liner grazed by a turbulent boundary layer . [Abstract] [PDF] [PDF Plus]

2. Shunji Enomoto, Tatsuya Ishii, Toshio Nishizawa, Hidemi Toh. Numerical Analysis of Acoustic Liner Performance in grazing flow . [Citation] [PDF] [PDF Plus]